WILEY

NMR IN BIOMEDICINE

RESEARCH ARTICLE OPEN ACCESS

Multi-Shot Diffusion Imaging Using Motion Compensation Diffusion Encoding Waveforms and EPI With Keyhole

Kévin Moulin[1,2] | Tyler Cork[3,4] | Thomas Troalen[5] | Kelvin Chow[6] | Daniel B. Ennis[3,4] | Pierre Croisille[1,2] | Magalie Viallon[1,2]

[1]CREATIS Laboratory, Univ. Lyon, UJM-Saint-Etienne, INSA, CNRS UMR 5520, INSERM 1294, Saint-Etienne, France | [2]Department of Radiology, University Hospital Saint-Etienne, Saint-Etienne, France | [3]Department of Radiology, Stanford University, Stanford, California, USA | [4]Division of Radiology, Veterans Administration Health Care System, Palo Alto, California, USA | [5]Siemens Healthineers France, Saint-Denis, France | [6]Siemens Healthineers USA, Chicago, USA

Correspondence: Magalie Viallon (magalie.viallon@creatis.insa-lyon.fr)

ABSTRACT

Motion-induced shot-to-shot phase variation and strong image aliasing artifacts are common in diffusion weighted imaging (DWI) multi-shot EPI (MS-EPI). Herein, motion-compensated diffusion encoding waveforms were used to minimize shot-to-shot phase variation, and an MS-EPI with Keyhole (MS-EPIK) trajectory was evaluated to mitigate image aliasing.

MS-EPI and MS-EPIK with non-motion compensated (M_0), first order (M_0M_1), and first & second order ($M_0M_1M_2$) motion-compensated diffusion encoding waveforms and a reference single-shot (SS-EPI) acquisition with M_0 diffusion encoding were acquired in vivo at 3T in five volunteers in the brain, liver, and heart. Mean diffusivity (MD) and fraction of anisotropy (FA) were reported in the brain and heart, and the apparent diffusion coefficient (ADC) in the liver.

No statistical differences in MD and FA between the SS-EPI, MS-EPIK, and MS-EPI when using the M0M1M2 waveform were found in white and gray matter. In the right liver lobe, statistical differences were found between the ADC of the SS-EPI and MS-EPIK using the M_0, M_0M_1, and $M_0M_1M_2$ waveforms ($p < 0.001$) and with MS-EPI using $M_0M_1M_2$ ($p < 0.001$). No differences were observed in MD and FA in the heart between SS-EPI, MS-EPI, and MS-EPIK in the heart.

MS-EPIK is less sensitive to image aliasing than MS-EPI approach but remains susceptible to image distortion. Overall, $M_0M_1M_2$ waveforms were found to be the best approach to mitigate shot-to-shot phase variation for MS-EPI in the brain, liver, and heart.

1 | Introduction

Diffusion weighted imaging (DWI) is a technique that probes the self-diffusion of water molecules within the tissue. DWI is usually acquired using a single-shot spin-echo echo planar imaging (SS-EPI) sequence with diffusion encoding gradients placed symmetrically on either side of the 180° refocusing pulse [1]. In this traditional implementation, DWI has been robustly applied to several organs [2–4]. Despite its speed and efficiency, SS-EPI images remain severely affected by image distortion due to B_0 inhomogeneities [5] and Nyquist ghosting [6]. Efficient phase corrections exist for Nyquist ghosting

---

Abbreviations: DWI, diffusion weighted imaging; SS-EPI, single-shot echo planar imaging; MS-EPI, multi-shot EPI; MS-EPIK, multi-shot EPI with keyhole; ACS, auto-calibration signal; GMN, gradient moment nulling; ADC, apparent diffusion coefficient; MD, mean DIFFUSIVITY; FA, fraction of anisotropy; RMSE, root mean square error; CV, coefficient of variation.

[7–9], while image distortion remains an active problem for modern SS-EPI.

B_0 off-resonances induce phase accrual during the EPI echo train that leads to image distortion along the phase-encoding direction [10]. This sensitivity to B_0 inhomogeneity is directly related to the EPI k-space traversal speed and the EPI gradient-echo train length duration (T_{EPI}). Retrospective image distortion correction has been proposed such as Blip-up Blip-down [11], BUDA [12], or B_0 mapping correction [5], but all require additional acquisitions. A simplistic way to reduce B_0 sensitivity is to directly shorten T_{EPI} by using high readout bandwidth, or parallel imaging [13,14], but both come at the expense of lower signal-to-noise ratio (SNR).

Echo train length duration can also be reduced by using multi-shot spin-echo EPI (MS-EPI), in which the k-space is acquired segmentally either in the readout [15] or phase direction [16]. The phase-encode segmented acquisition results in a lower number of k-space lines acquired per shot, hence a shorter T_{EPI}. However, the interaction between diffusion-encoding gradients and physiological motion leads to shot-to-shot phase variations and image aliasing that has limited the use of MS-EPI for DWI.

Several retrospective reconstruction methods have been proposed to reduce shot-to-shot phase variation. Simple linear phase variations can be corrected by re-acquiring a 2D low spatial resolution navigator after each shot [17,18]. Multiplexed sensitivity-encoding (MUSE) is a navigator-free method where each shot is first reconstructed by a parallel imaging SENSE approach and phase corrected [19]. An alternative approach is the local low-rank method [20,21], which is an iterative approach that can handle more complex phase variation and a higher number of shots than MUSE. However, the iterative process may lead to longer reconstruction times and is subject to extensive ad hoc tuning for good convergence.

Only a few prospective approaches have been evaluated to limit shot-to-shot phase variation [22,23] in DWI MS-EPI. Advanced diffusion encoding gradient waveform designs, such as gradient moment nulling (GMN) [24], may be used to reduce the sensitivity of diffusion encoding to unwanted physiological motion. Diffusion encoding waveforms designed using GMN null the phase accumulated during the diffusion encoding for a given order of motion, but high-order GMN designs lead to an increased TE for an equivalent b-value compared to a non-motion compensated M_0 waveform. Traditional monopolar diffusion encoding waveforms are non-motion compensated and zero-order nulled (M_0). First-order nulled waveforms (M_0M_1), designed for velocities compensation, have been showed to successfully reduce the cardiac motion sensitivity in liver DWI and remove unwanted signal loss in the left liver lobe [25–27]. First & second order ($M_0M_1M_2$) nulled moment designs, which compensate for velocities and accelerations, have been shown to successfully compensate for cardiac motion and enable motion-free cardiac diffusion imaging [28–30].

Alternative strategies to SS-EPI readout have been proposed such as EPI with keyhole (EPIK) [31]. With EPIK readout, the k-space is under-sampled in the high frequency k-space regions and fully sampled near the k-space center (i.e. keyhole).

In multi-shot EPIK (MS-EPIK), the readouts acquire more lines per shot than traditional MS-EPI but fewer than SS-EPI. Previous work has investigated the readout keyhole region as a self-navigated technique to correct inter-shot phase variation in DWI MS-EPI [32]. Due to its unique k-space trajectory, MS-EPIK is more robust to image aliasing.

In this work, we proposed to evaluate prospective strategies to reduce shot-to-shot phase variation for interleaved phase-segmented MS-EPI. We hypothesized that shot-to-shot phase variations are due to physiological motion that can be approximated with constant velocity and/or constant acceleration during the diffusion encoding and thus can be mitigated with motion-compensated diffusion encoding. The **first objective** of this work was to investigate M_0M_1 and $M_0M_1M_2$ motion-compensated diffusion gradient waveforms as a prospective way to reduce shot-to-shot phase variation in MS-DWI. The **second objective** was to investigate the capabilities of MS-EPIK for mitigating inter-shot phase variation and image aliasing. In silico and in vivo comparisons between SS-EPI, MS-EPI, and MS-EPIK using M_0, M_0M_1, and $M_0M_1M_2$ diffusion encoding waveforms were shown in the brain, liver, and heart.

2 | Theory

2.1 | EPIK for MS DWI

In an SS-EPI trajectory, all k-space lines (N_{lin}) are sampled in a single shot by using a gradient echo train of alternating polarities and small phase-encoding "blip" gradients. In a phase-interleaved MS-EPI trajectory, the gradient echo-train sub-samples the k-space by using larger phase-encoding blip gradients. The acquisition is repeated N_{shot} times to completely fill the k-space. The duration of the echo-train length (T_{EPI}) is divided by N_{shot} compared to an SS-EPI trajectory (Figure 1A), which leads to a lower T_{EPI}; hence, MS-EPI trajectories have a lower phase build-up due to B_0 inhomogeneities compared to SS-EPI.

EPIK is an EPI trajectory in between SS-EPI and MS-EPI. It was proposed initially by Zaitsev et al. [31] and has been principally use for fMRI [33] and perfusion imaging [34]. It has only been evaluated in a few DWI studies [32]. EPIK readout trajectories are composed of large phase-encoding blip gradients in the high-frequency regions of k-space and low blip gradients in the central part of k-space, the keyhole (Figure 1B). EPIK trajectories can be seen as having extra central k-space lines compared to MS-EPI trajectory or fewer lines than an SS-EPI one. It is thus expected that EPIK presents a higher sensitivity to field inhomogeneities than MS-EPI, but lower than SS-EPI [31].

Multi-shot EPIK (MS-EPIK) acquires high frequencies k-space lines for interleaving and fully samples the keyhole region for each shot. In this work, the MS-EPIK trajectories were constructed by adding extra central k-space lines compared to an interleaved MS-EPI trajectory. The extra lines were added to fill the gap between four interleaved k-space lines placed symmetrically from the center of the k-space. With the MS-EPIK trajectory, $4\times(N_{shot}-1)$ extra k-space lines were sampled at the center of the k-space compared to the MS-EPI trajectory. With
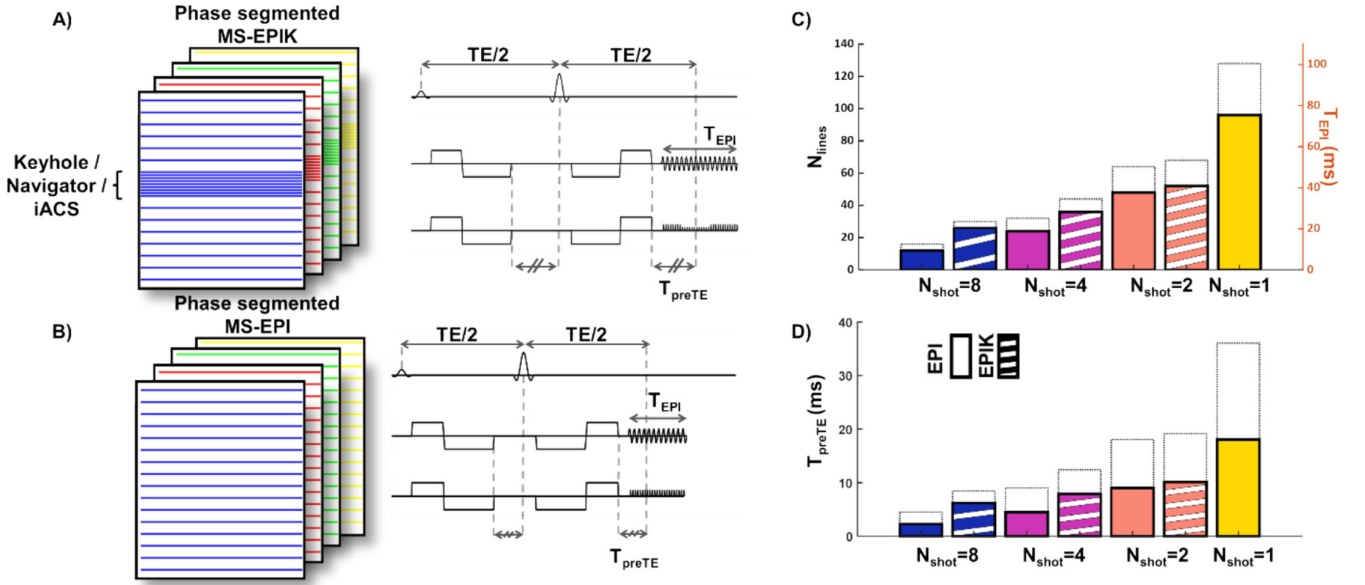
FIGURE 1 | Sequence diagrams and k-space trajectories of (A) Multi-shot EPI with Keyhole (MS-EPIK) and (B) EPI (MS-EPI) readouts. The duration of the EPI readout (T_{EPI}) and the contribution of the EPI readout to the TE (T_{preTE}) are proportional to the number of k-space lines (N_{lin}) in the EPI echo train and thus inversely proportional to the number of shots (N_{shot}). (C) N_{lin} and T_{EPI} as a function of N_{shot} for the MS-EPI and MS-EPIK readout. (D) N_{lin} and T_{EPI} as a function of N_{shot} for the MS-EPI and MS-EPIK readout. T_{preTE} as a function of N_{shot} for the MS-EPI and MS-EPIK readouts. All diagrams are given for a matrix of 128×128, a bandwidth of 2056 Hz/pixel, and a partial Fourier factor of 75%. For plots (C) and (D), the dotted lines represent the case without partial Fourier.

this design, the polarity of the same keyhole line is expected to change between odd and even shots. In this work, these polarities changes were only considered during the Nyquist phase correction step.

Since the keyhole region is sampled for each MS-EPIK shot, it can be used for self-navigation [32]. Additionally, the keyhole region can also be used as an internal auto-calibration signal (ACS) for GRAPPA [13] parallel imaging reconstruction. Since these ACS lines are shared across shots, they can also be used to calibrate a multi-dimensional GRAPPA approach operating on the channels and shot dimensions (GRAPPA C + S). GRAPPA C + S has been previously demonstrated as a robust shot-to-shot phase mitigation technique for MS-EPI [35].

In this work, SS-EPI, MS-EPI, and MS-EPIK trajectories were compared. The effect of image aliasing artifacts due to shot-to-shot phase variation and image acceleration were also studied using GRAPPA with external ACS lines, internal ACS lines, and GRAPPA C + S.

2.2 | Motion Compensation Designs

In the diffusion encoding experiment, the water molecules' microscopic displacements are encoded in the phase of magnetization. For stationary objects, the intra-voxel phase distribution due to diffusion is a zero-centered Gaussian with a nulled phase, which generates a signal attenuation at a voxel scale. Macroscopic physiological bulk motions can affect the intra-voxel phase distribution. If the bulk motion is coherent (equivalent for all molecules within the voxel), then, the intra-voxel phase distribution is simply shifted and thus encoded in

the phase of the MR signal with no contribution to the magnitude. For single-shot imaging, generally only magnitude images are used to extract diffusion information. However, for MS-EPI subtly different coherent motion contributes to the shot-to-shot phase variation and generates signal aliasing. More complex kind of motion, (i.e. cardiac motion where tissue deformation is involved) may strongly modify the intra-voxel phase distribution and lead to unwanted signal attenuation at a voxel scale [36,37].

Advanced diffusion encoding gradient waveforms have been proposed to remove the phase contribution of the physiologic motion while preserving the diffusion information [28,29]. These waveforms have been designed using the GMN theory [24]. We can define M_n, where n is the order of the moment nulling for the diffusion encoding waveform $G(t)$:

$$M_n = \int_o^T G(t)t^n . dt \qquad (1)$$

By designing the waveform $G(t)$ such that M_n is nulled, the corresponding order of motion will have no phase contribution at the end of the diffusion encoding. To be able to make an image, all diffusion encoding waveforms must have at least a zero-order moment nulled $M_0 = 0$. A waveform designed so that both M_0 and M_1 are nulled and will compensate for all spin motion with a constant velocity during the diffusion encoding, regardless of the velocity magnitude. A waveform with M_0, M_1, and M_2 nulling will compensate for the phase of spins that have a constant velocity or the spins that have a constant acceleration during the diffusion encoding. The strong assumption behind the GMN theory is that the spins motion trajectories can be fully described

by a constant velocity or a constant acceleration during the entire diffusion encoding waveform.

In this work, all diffusion-encoding waveforms were designed with trapezoidal gradients at the maximum amplitude G_{max} (Figure 2A). Three waveforms were evaluated: a non-motion compensated monopolar approach, M0 nulled (M_0), with a pair of gradient waveforms of the same duration (D1) and same polarity (11) on each side of the refocusing pulse; a bipolar velocity compensated approach (M_0M_1), with two pairs of gradients lobes of the same duration D1, but with opposite polarity ($1\underline{1}1\underline{1}$) on each side of the refocusing pulse; and a velocity and acceleration compensated gradient waveform ($M_0M_1M_2$) with two pairs of gradient lobes with duration D1 and D2 and mirrored polarity across the refocusing pulse ($1\underline{2}2\underline{1}$).

As shown in Figure 2B, the maximum b-value available for each diffusion encoding waveform is strongly dependent on the duration of the EPI train length before the echo (T_{preTE}), which is the portion of the EPI that contributes the most to the minimum TE available. For an equivalent T_{preTE}, a non-motion-compensated approach can reach a higher b-value (or a lower TE for an equivalent b-value). Reducing T_{Epi} by reducing the number of lines N_{lin}/shot, using high readout bandwidth, or using parallel imaging usually reduces T_{preTE}. Another way to reduce T_{Epi} and/ or T_{preTE} is to employ the Partial Fourier method [38]. With PF, a portion of k-space is not acquired, leading to lower N_{lin}/shot and a shorter T_{Epi} and T_{preTE} (Figure 1C,D). However, since the k-space lines are removed before the echo, PF predominantly reduces T_{preTE} thus allowing higher b-values and/or a lower TE

for a given diffusion encoding waveform. Although PF allows a lower T_{Epi} and T_{preTE}, the k-space traveling speed remains unchanged, thus, the PF approach does not provide benefit regarding B_0 inhomogeneities and image distortion. Additionally with PF, the presence of significant motion can generate phase inconsistencies between acquired and conjugate k-space points, resulting in signal dropout [39]. Figure 2C shows the link between TE and N_{shot} for a b-value of 1000 s/mm² for SS-EPI, MS-EPI, and MS-EPIK readout using a PF of 75% and for the three diffusion-encoding waveforms studied here.

3 | Methods

3.1 | Numerical Simulations

In silico numerical simulations were performed in MATLAB (R2023, The Mathworks, Natick, USA) using homemade scripts to evaluate shot-to-shot phase variation, B_0 inhomogeneities, and acceleration capabilities between MS-EPI and MS-EPIK readouts. All simulations were performed using a Shepp-Logan phantom [40] on a 128×128 matrix acquired with 26 channels, a Partial Fourier of 75%, and a readout bandwidth of 1780 Hz. SS-EPI, MS-EPI, and MS-EPIK readouts with $N_{shot} = 2,4,8$ were simulated. Considering partial Fourier, the SS-EPI trajectory had 96 lines; MS-EPI had 48, 32, and 16 lines per shot for $N_{shot} = 2,4,8$, respectively; MS-EPIK had 56, 40, and 24 lines per shot for $N_{shot} = 2,4,8$, respectively. Simulations were noiseless and T1, T2, and T2* relaxations were not considered.
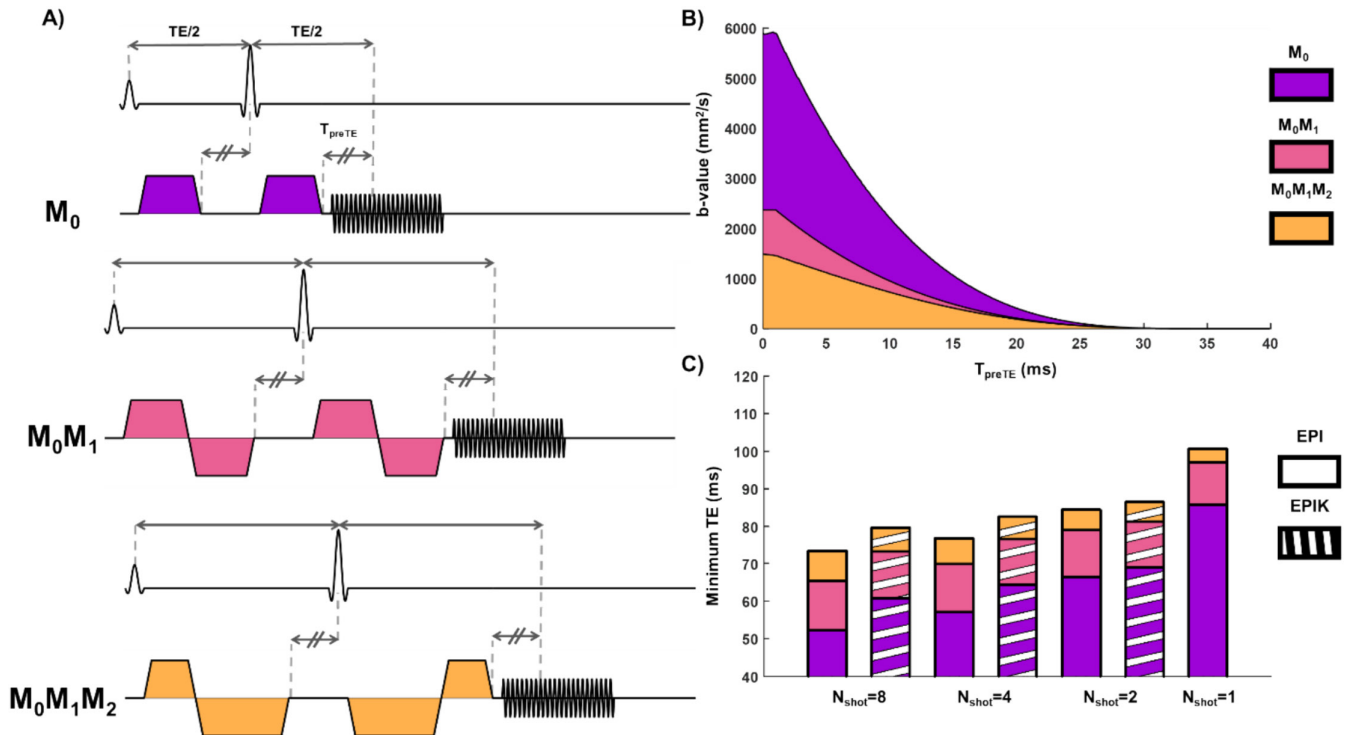

FIGURE 2 | (A) Sequence diagram of non-motion compensated (M_0), first order (M_0M_1), and first & second ($M_0M_1M_2$) order motion compensated diffusion encoding. (B) Maximum b-value as a function of T_{preTE} for each diffusion encoding waveform. The maximum b-value is dependent of T_{preTE} because it impacts the maximum time available to apply the diffusion encoding gradient. (C) Minimum TE as a function of the number of shots (N_{shot}), the three diffusion encoding waveforms, and for the MS-EPI and MS-EPIK readouts. All diagrams are given for a matrix of 128×128 and a bandwidth of 2056 Hz/pixel and a partial Fourier factor of 75%. For plot (C), a fixed b-value of 1000 s/mm² was used.

Physiological motion was not directly simulated by instead emulated as shot-to-shot phase variation by incrementing the phase of each shot by pi/3. B_0 inhomogeneities were emulated by adding a bi-linear (diagonal) off-resonance gradient of 400 Hz in the top left corner and zero in the bottom right corner of the image. The B_0 inhomogeneities were applied to the k-space by generating intra-line dephasing by emulating the timing of the gradient echo-train readout. Finally, parallel imaging reconstruction using the GRAPPA method [13] was evaluated using acceleration factors of 2, 4, and 8 by only considering a sub-set of shots and by reconstructing the missing lines. Details for the GRAPPA reconstructions are given in the Image Reconstruction and Acceleration section below.

3.2 | In Vivo Acquisitions

Five healthy volunteers ($N = 5$) were scanned on a 3T scanner (MAGNETOM Prisma, Siemens Healthcare, Erlangen, Germany) after being given signed statements of informed consent and were recruited according to the protocol approved by the Institutional Review Boards (#2015-A01802-47, CPP Nord Ouest VI, #19.02.22, and CPP Ile de France VIII, #20 04 05), in agreement with the principles in the Declaration of Helsinki. DWI with both MS-EPI and MS-EPIK readouts ($N_{shot} = 4$) with M_0, M_0M_1, and $M_0M_1M_2$ diffusion encoding waveforms and a reference SS-EPI acquisition were acquired in the brain and the liver. SS-EPI and both MS-EPI and MS-EPIK ($N_{shot} = 4$) were acquired in the heart using an $M_0M_1M_2$ diffusion encoding waveform. The main sequence parameters were kept identical across organs (field of view [FOV] = $300 \times 300 mm^2$, matrix = 128×128, Partial Fourier = 6/8, slice thickness = 5 mm, bandwidth = 2056 Hz/px). The b-values, number of slices, and the physiological synchronization were adjusted per organ and TE was minimized for a given readout and a given diffusion encoding waveform. The comparisons between SS and MS were done for a fixed acquisition time by adjusting the number of averages: $N_{avg} = 8$ for SS-EPI and $N_{avg} = 2$ for the $N_{shots} = 4$ MS-EPI and MS-EPIK readouts. Detailed sequence parameters are found in Table 1.

TABLE 1 | Sequence parameters.

	Brain			Liver			Heart		
Resolution (mm³)	$2 \times 2 \times 5$			$2 \times 2 \times 7$			$2 \times 2 \times 7$		
Matrix (reconstructed)	128×128			128×128			128×128		
PF (%)	75			75			75		
BW (Hz/pixel)	1700			1700			1700		
Echo spacing (ms)	0.69			0.69			0.69		
Number of Slices	7			5			1		
B value (s/mm²)	0–1000			0–350			0–350		
Nb of DWI directions	6			6			6		
Synchronization	None			None			ECG and Respiratory navigator		
TR (ms)	2000			2000			1 respiratory cycle (~4000 ms)		
Scan time (min)	2 min			2 min			4 min		
	SS	MS-EPI	MS-EPIK	SS	MS-EPI	MS-EPIK	SS	MS-EPI	MS-EPIK
N_{lin}/shot	96	24	36	96	24	36	96	24	36
N_{shot}	1	4	4	1	4	4	1	4	4
N_{ave}	8	2	2	8	2	2	8	2	2
N_{lin} keyhole/internal ACS/ navigator	0	0	12	0	0	12	0	0	12
T_{preTE} (ms)	11.2	6.7	10.8	11.2	6.7	10.8	11.2	6.7	10.8
T_{EPI} (ms)	32	17	25.3	32	17	25.3	32	17	25.3
PE Bandwidth (Hz)	30.2	60.4	40.3	30.2	60.4	40.3	30.2	60.4	40.3
TE (ms)									
M_0	47	40	46	47	33	40			
M_0M_1		64	72		52	61			
$M_0M_1M_2$		66	73		55	59	65	55	59

3.3 | Image Reconstruction and Acceleration

Raw data were extracted after inline Nyquist phase correction [9] using the FIRE framework [41]. All further reconstruction and analysis were performed offline in MATLAB (R2023, The Mathworks, Natick, USA).

Two types of image reconstruction were performed in this work: a "naïve" and an accelerated approach. The naïve approach was performed by simply merging the interleaved k-space lines across shots obtained from MS-EPI or MS-EPIK acquisitions. For MS-EPIK, the k-space lines that overlapped across shots in the keyhole region were averaged. The accelerated reconstructions were performed using the GRAPPA method [13]. For each acquisition, 24 external ACS lines were acquired for external GRAPPA reconstructions. For the MS-EPIK acquisitions internal GRAPPA and GRAPPA C + S reconstructions [35] were proposed by using the keyhole lines as internal ACS lines. ACS lines were used to estimate the weight of a 5×3 GRAPPA kernel.

The diffusion post-processing consisted of two steps: First, the magnitude of the signal was averaged over the N_{avg} acquired. Second, a diffusion tensor imaging (DTI) model was applied for brain and heart scans and an apparent diffusion coefficient (ADC) model was applied for the liver scans. The mean diffusivity (MD), the fraction of anisotropy (FA), and the primary Eigen orientation (E1) were extracted from the DTI model. For cardiac acquisitions, E1 corresponds to the aggregate cardiomyocyte orientation.

3.4 | Quantitative Analysis

For the in silico numerical simulations, the Root Mean Square Error (RMSE) between the simulated image and the Shepp-Logan ground truth image was calculated after signal intensity normalization. Spatial differences of MD and FA compared to reference were analyzed in the DWI Shepp-Logan phantom after DTI modeling.

For in vivo acquisitions, ADC, MD, and FA values were reported as mean ± standard deviation (SD) per slice after manual segmentation of the brain, right liver lobe, and the heart's left ventricle. The brain was further divided based on the FA [42]: the tissue with FA ≥ 0.3 was considered as white matter and the tissue with FA < 0.3 were considered as gray matter. Statistical differences were evaluated using an ANOVA considering the SS-EPI acquisition as a reference scan. Values of $p < 0.05$ were considered significant.

A shot-to-shot phase variation analysis was studied using the phase of each individual shot reconstructed from the keyhole region of the EPIK acquisitions. The phase was extracted from the multi-channel data by using the highest weight of a coil compression method [43]. The inter-shot phase coefficient of variation (CV) was calculated for each organ and each diffusion encoding waveform. The CV was calculated pixel-wise within the ROI by dividing the inter-shot phase SD by the inter-shot phase mean.

For the in vivo accelerated reconstruction, SNR was calculated using the image difference method for accelerated reconstruction as described by Goerner and Clarke [44].

4 | Results

4.1 | In silico shot-to-shot phase variation analysis

The shot-to-shot phase variation analysis on a numerical phantom for SS-EPI, MS-EPI, and MS-EPIK with $N_{shot} = 2,4,8$ is shown in Figure 3A. The SS-EPI readout is not affected by the shot-to-shot phase variation and provides an RMSE of 3.7% relative to the numerical phantom. For the MS-EPI readout, the phase variation between shots generates distinct aliasing in the final image. As N_{shot} increases, the number of aliasing ghosts and the RMSE increase. For the MS-EPIK readout, since the center portion of k-space is reacquired with each shot, the aliased signal has a lower intensity which leads to a lower RMSE than for MS-EPI at equivalent N_{shot}.

4.2 | In Silico B0 Inhomogeneity Analysis

In silico images of SS-EPI, MS-EPI, and MS-EPIK readout at $N_{shot} = 2,4,8$ simulated in the presence of B_0 inhomogeneities are given in Figure 3B. Since image distortion is related to T_{epi}, the SS-EPI image is the most distorted with an RMSE of 17.1% compared to ground truth. For MS-EPI, the image deformation and RMSE reduce as N_{shot} increase and is as low as 7.2% for $N_{shot} = 8$. In the case of MS-EPIK, the RMSE is constant at 15% for any N_{shot} since more central k-space lines are sampled than for MS-EPI.

4.3 | In Silico Acceleration Analysis

Examples of naïve, internal GRAPPA, external GRAPPA, and GRAPPA C + S reconstructions with $R = 2,4,8$ for $N_{shot} = 8$ EPI and EPIK readouts are shown in Figure 4A. In the naïve reconstruction of MS-EPI, the aliasing increases as R increases while the MS-EPIK reconstructions show robustness to aliasing.

RMSE for each reconstruction is given in Figure 4B. Similar RMSE were found between GRAPPA C + S and internal GRAPPA reconstruction. At $N_{shot} = R$, the GRAPPA C + S method operates only on the coil dimension and behaves exactly like the internal GRAPPA approach.

4.4 | In Vivo Acquisition

Examples of in vivo acquisitions for the brain, liver, and heart are shown in Figure 5. In the brain, image distortions due B0 inhomogeneities are visible in the frontal lobe (blue arrow) when using SS-EPI. Image distortions were reduced when using MS-EPI but still present when employing MS-EPIK. Image aliasing due to shot-to-shot phase variations (red and orange arrow) were visible in all subjects when using M_0 or M_0M_1 for both MS-EPI and MS-EPIK readout. Aliasing-induced artifacts were visible in the colored FA with a wrong orientation of the fibers being shown in the side lobes. Aliasing were strongly reduced when using $M_0M_1M_2$ motion-compensated diffusion encoding waveforms and colored FA were equivalent to the SS-EPI ones. For the free-breathing liver acquisitions, aliasing due to shot-to-shot phase variations were observed on all volunteers when using M_0 and M_0M_1
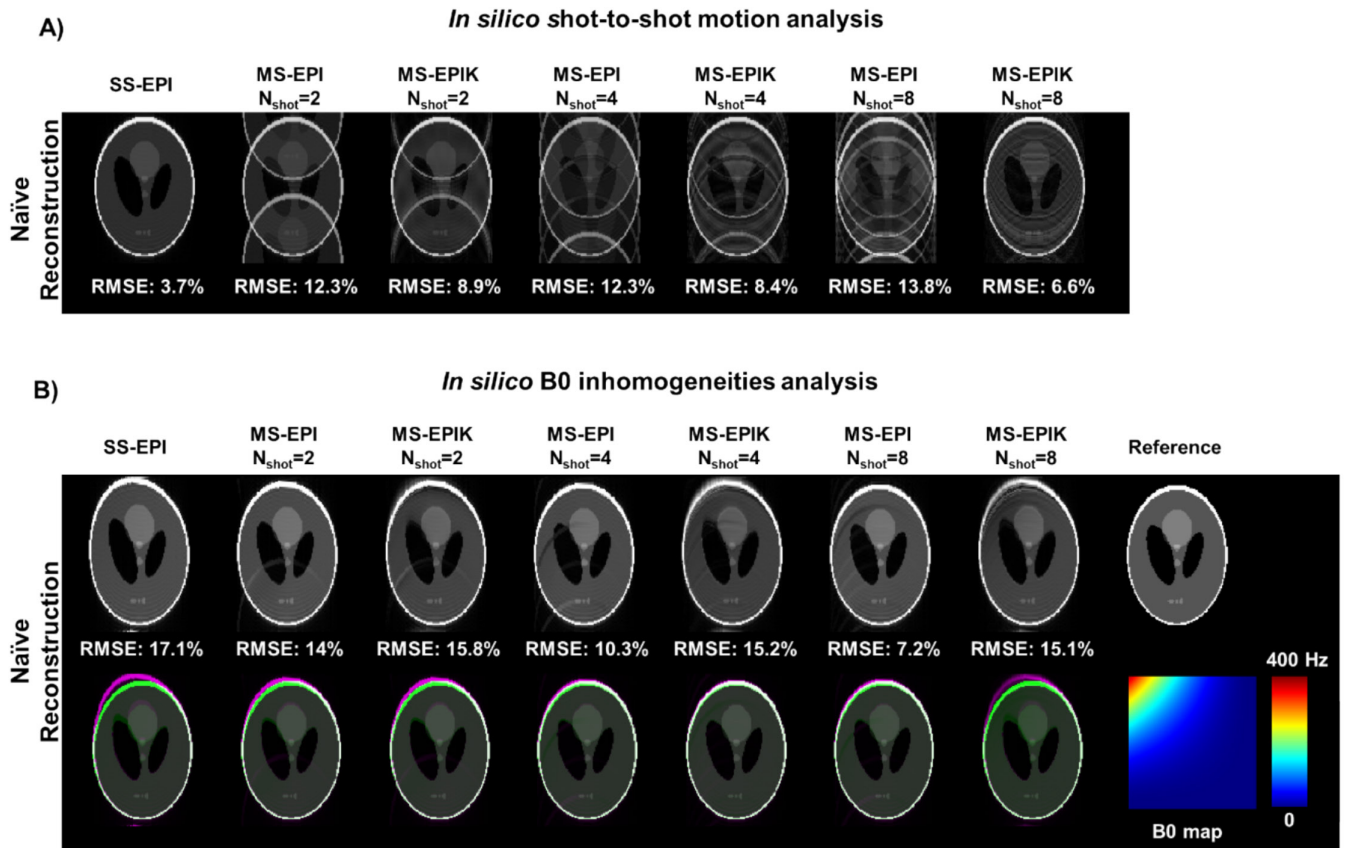
FIGURE 3 | In silico motion and B_0 inhomogeneities analysis. A) Simulated shot-to-shot phase variation in a numerical Shepp-Logan phantom for Single-shot EPI (SS-EPI) and multi-shot EPI (MS-EPI) and EPIK (MS-EPIK) readouts. A constant phase was added to each shot to emulate motion-induced shot-to-shot phase variation. B) Simulated B_0 inhomogeneities in a numerical Shepp-Logan phantom for SS-EPI, MS-EPI, and MS-EPIK readouts. For A) and B) the root mean square errors (RMSE) are calculated from a non-distorted Shepp-Logan reference after signal normalization. Overall, lower RMSE was obtained for MS-EPIK compared to MS-EPI in the motion analysis. For the B0 inhomogeneities analysis, for all N_{shot}, higher RMSE was measured for the MS-EPIK compared to MS-EPI.

waveforms with either MS-EPI or MS-EPIK which affected the corresponding ADC maps. Aliasing artifacts were less marked in acquisitions performed using $M_0M_1M_2$ waveforms with MS-EPI and MS-EPIK. In the heart, image distortions in the inferolateral wall due to B0 inhomogeneities in the heart/lung/liver interface were visible in all subjects when using SS-EPI (blue arrow). Distortions were strongly reduced when using MS-EPI compared to MS-EPIK and SS-EPI. No significant aliasing was observed in both MS-EPIK and MS-EPI hearts acquisitions across volunteers.

Quantitative comparisons of MD, FA, and ADC for the three organs are given in Figure 6. Diffusion parameters reported per subject are also given in Supplementary Material—Table S1. Across slices and volunteers, an MD of $0.76 \pm 0.04 \times 10^{-3}\,\mathrm{mm^2/s}$ and $1.02 \pm 0.17 \times 10^{-3}\,\mathrm{mm^2/s}$ was measured in the white and gray matter respectively using the SS-EPI and the non-motion compensated waveform M_0. Statistical significant increases compared to SS-EPI were observed in MD in white matter when employing MS-EPI with M_0 and M_0M_1 waveforms ($0.98 \pm 0.12 \times 10^{-3}\,\mathrm{mm^2/s}$, $p < 0.001$; $0.91 \pm 0.23 \times 10^{-3}\,\mathrm{mm^2/s}$, respectively) and MS-EPIK with M_0 and M_0M_1 ($1.09 \pm 0.15 \times 10^{-3}\,\mathrm{mm^2/s}$ vs. $0.98 \pm 0.16 \times 10^{-3}\,\mathrm{mm^2/s}$, $p < 0.001$, respectively). Similar increases compare to SS-EPI were observed in gray matter with

MS-EPI M_0 and M_0M_1 waveforms ($1.23 \pm 0.23 \times 10^{-3}\,\mathrm{mm^2/s}$, $p < 0.001$; $1.23 \pm 0.23 \times 10^{-3}\,\mathrm{mm^2/s}$, $p < 0.001$, respectively) and MS-EPIK with M_0 and M_0M_1 ($1.43 \pm 0.23 \times 10^{-3}\,\mathrm{mm^2/s}$, $p < 0.001$; $1.36 \pm 0.28 \times 10^{-3}\,\mathrm{mm^2/s}$, $p < 0.001$, respectively). The FA was 0.44 ± 0.04 in white matter and 0.15 ± 0.02 in gray matter using the SS-EPI and M_0. No statistical differences were found in FA for white matter across measurements. For the gray matter, significant increases were found for FA measured with MS-EPI using M_0, M_0M_1, and $M_0M_1M_2$ waveforms (0.21 ± 0.02, $p < 0.001$; 0.20 ± 0.03, $p < 0.001$; 0.17 ± 0.03, $p < 0.001$, respectively) and MS-EPIK using M_0 and M_0M_1 (0.22 ± 0.02, $p < 0.001$; 0.19 ± 0.03, $p < 0.001$, respectively).

An ADC of $1.40 \pm 0.18 \times 10^{-3}\,\mathrm{mm^2/s}$ has been found in the right liver lobe using the SS approach. Significant increases were found with MS-EPIK using the M_0, M_0M_1, $M_0M_1M_2$ waveforms ($2.05 \pm 0.69 \times 10^{-3}\,\mathrm{mm^2/s}$, $p < 0.001$; $1.79 \pm 0.46 \times 10^{-3}\,\mathrm{mm^2/s}$, $p < 0.001$, respectively) while the ADC decreases using $M_0M_1M_2$ with MS-EPI and MS-EPIK ($0.98 \pm 0.28 \times 10^{-3}\,\mathrm{mm^2/s}$, $p < 0.001$; $0.84 \pm 0.39 \times 10^{-3}\,\mathrm{mm^2/s}$, $p < 0.001$).

In the heart, no statistical differences were observed between MD measured with SS-EPI ($1.42 \pm 0.06 \times 10^{-3}\,\mathrm{mm^2/s}$) against MS-EPI and MS-EPIK ($1.50 \pm 0.14 \times 10^{-3}\,\mathrm{mm^2/s}$, $p = 0.47$; $1.55 \pm 0.13 \times 10^{-3}\,\mathrm{mm^2/s}$, $p = 0.16$, respectively). Similarly, no
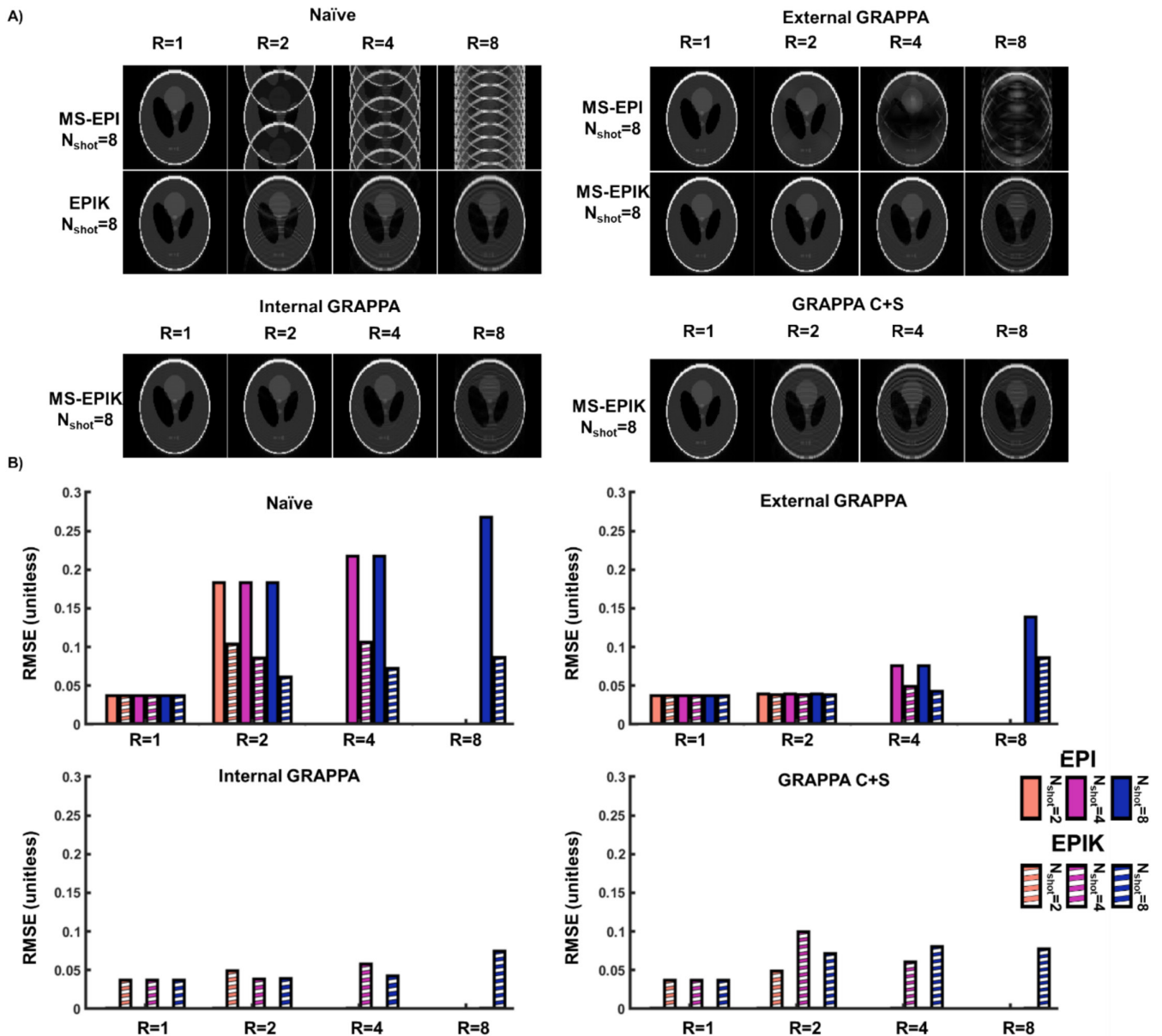
FIGURE 4 | In silico acceleration analysis. (A) Simulated Shepp-Logan for different acceleration factors (R) for the multi-shot EPI (MS-EPI) and EPIK (MS-EPIK) readouts and reconstructed the naïve, external GRAPPA, internal GRAPPA, and GRAPPA C + S approaches. (B) Root-mean-square error (RMSE) as a function of R and the number of shots (N_{shot}) for MS-EPI, MS-EPIK, and four reconstructions methods. Overall, lower RMSE was obtained for the MS-EPIK compared to MS-EPI.

difference was found for FA between SS-EPI, MS-EPI, and MS-EPIK (0.41 ± 0.04; 0.40 ± 0.04, $p = 0.77$; 0.42 ± 0.02, $p = 0.78$, respectively).

4.5 | In Vivo Shot-To-Shot Phase Variation Analysis

An example of shot-to-shot phase variation in the brain phase map is given in Figure 7. Additional phase maps in the brain, liver and heart can be found in Supplementary Material—Figure S1. Using the keyhole region of an EPIK readout, a low-resolution image can be obtained at each shot and the phase can be resolved as shown in Figure 7A. For all waveforms, the phase variation was diffusion direction dependent and was minimum for the non-diffusion weighted images

(Figure 7B). The non-motion compensated diffusion encoding waveform M_0 presents large phase variation between shots with a CV of $93.4 \pm 33.2\%$ in the brain and $163.3 \pm 89.0\%$ in the right liver lobe. For $M_0 M_1$, the CV was reduced to $52.0 \pm 14.8\%$ and $147.8 \pm 104.1\%$ in the brain and liver, respectively. Finally, $M_0 M_1 M_2$ waveforms acquisitions had the lowest phase variation with $27.6 \pm 11.5\%, 139.0 \pm 97.2\%$, and $40.5 \pm 12.1\%$ in the brain, liver, and heart, respectively.

4.6 | In Vivo Acceleration Analysis

An example of liver reconstruction using the $M_0 M_1 M_2$ waveform for different GRAPPA models and different acceleration factors for MS-EPI and MS-EPIK readout is shown in Figure 8.
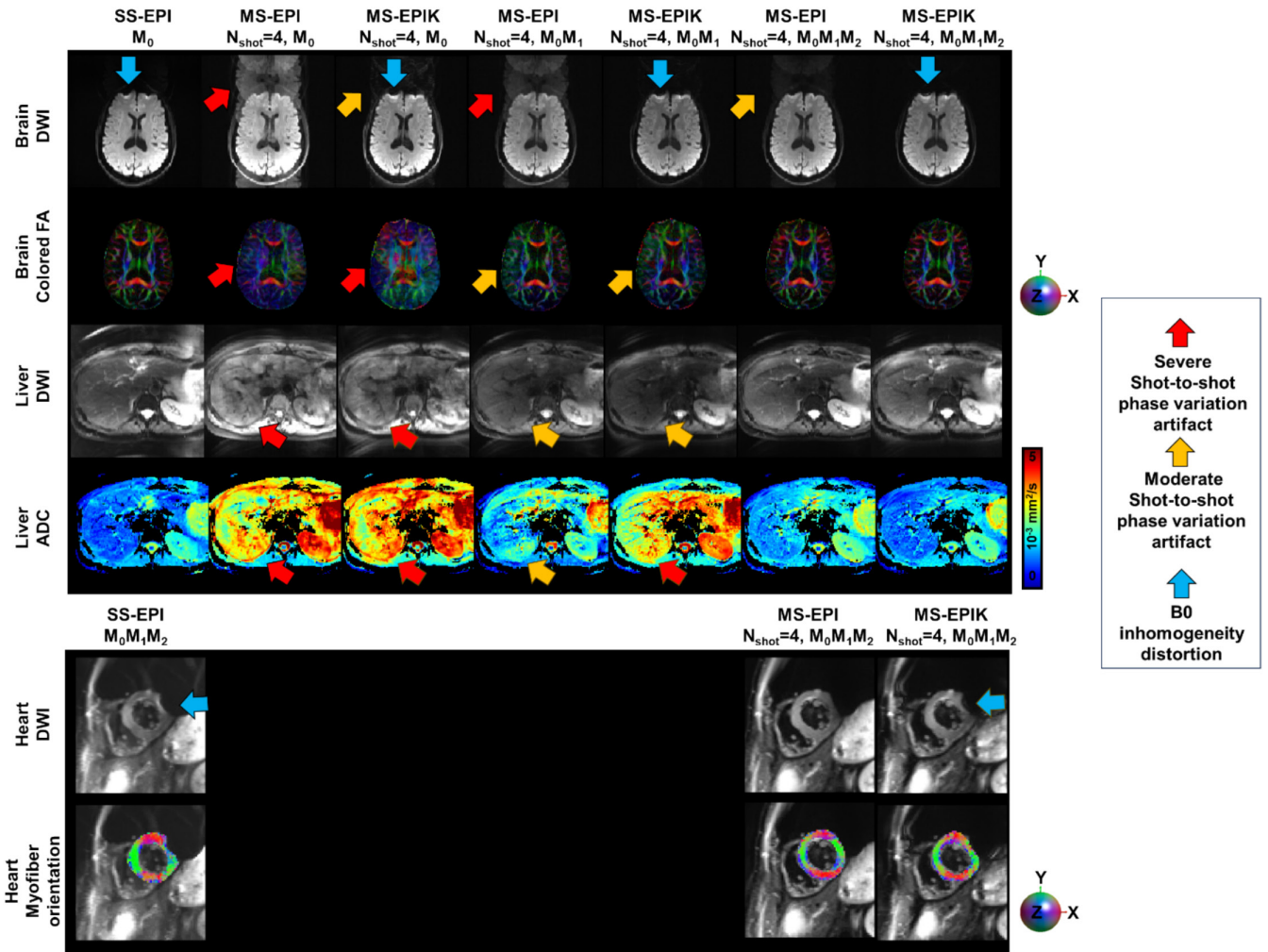
FIGURE 5 | Example of in vivo images in one volunteer of the brain, liver, and heart with a naïve reconstruction for the non-motion compensated (M_0) and motion compensated (M_0M_1 and $M_0M_1M_2$) diffusion encoding waveforms and for the single-shot EPI (SS-EPI) and multi-shot EPI (MS-EPI) and EPIK (MS-EPIK) acquisitions. Diffusion-weighted images (DWI) are shown for each organ as well as the colored fraction of anisotropy (FA) for the brain, Apparent Coefficient of Diffusion (ADC) for the liver, and the primary Eigen orientation (E1 or aggregate cardiomyocyte orientation) in the heart. SS-EPI are acquired without motion compensation (M_0) for the brain and liver and with second-order motion compensation ($M_0M_1M_2$) for the heart.

The naïve reconstructions at $R = 1$ have more aliasing artifacts with MS-EPI compared to the MS-EPIK acquisition, indicating more shot-to-shot phase variation. At higher R, the MS-EPIK readout shows limited aliasing. The GRAPPA C + S reconstruction provides good phase mitigation at $R = 1$. At $R = 2$, the image reconstructed using external or internal GRAPPA reconstruction displays shot-to-shot phase variation aliasing, while none are visible for the GRAPPA C + S method. At $R = 4$ only one shot is used in the reconstruction, no inter-shot phase aliasing artifacts are visible.

Quantitative SNR comparisons are given in Figure 9. Three effects may affect the SNR in this analysis: 1) the shot-to-shot phase variation and corresponding signal aliasing; 2) the lower SNR of parallel imaging at a higher acceleration factor; 3) the TE differences between the diffusion encoding waveforms. In the brain and liver, at $R = 1$ and $R = 2$, higher SNR is obtained for the higher order motion compensated waveforms for the Naïve, internal, and external GRAPPA reconstruction (green arrows).

In these cases, the motion compensation provides an SNR benefit by reducing the shot-shot phase variation. At $R = 4$, only one shot is considered for reconstruction and thus there is no shot-to-shot phase variation issue. In this scenario, the motion compensated waveform provides little benefit and the higher TE of the motion-compensated diffusion waveform dominates the SNR (red arrows). In the brain, the GRAPPA C + S approach efficiently provides shot-to-shot phase mitigation with an overall SNR higher than the other reconstruction methods and thus the TE effect is predominant (red arrows). In the liver, the benefit of GRAPPA C + S was limited, and similar SNR was observed compared to external and internal GRAPPA. Overall, in the brain and liver, a higher SNR was obtained for the external and internal GRAPPA reconstruction at $R = 4$ compared to $R = 2$, showing that the shot-to-shot phase variation effect was more important than the reduced SNR of a higher R. In the heart, only the $M_0M_1M_2$ waveform was used and a higher R yielded a lower SNR showing little shot-to-shot phase variation effect. Thus, the highest SNR was obtained for the naïve reconstruction.
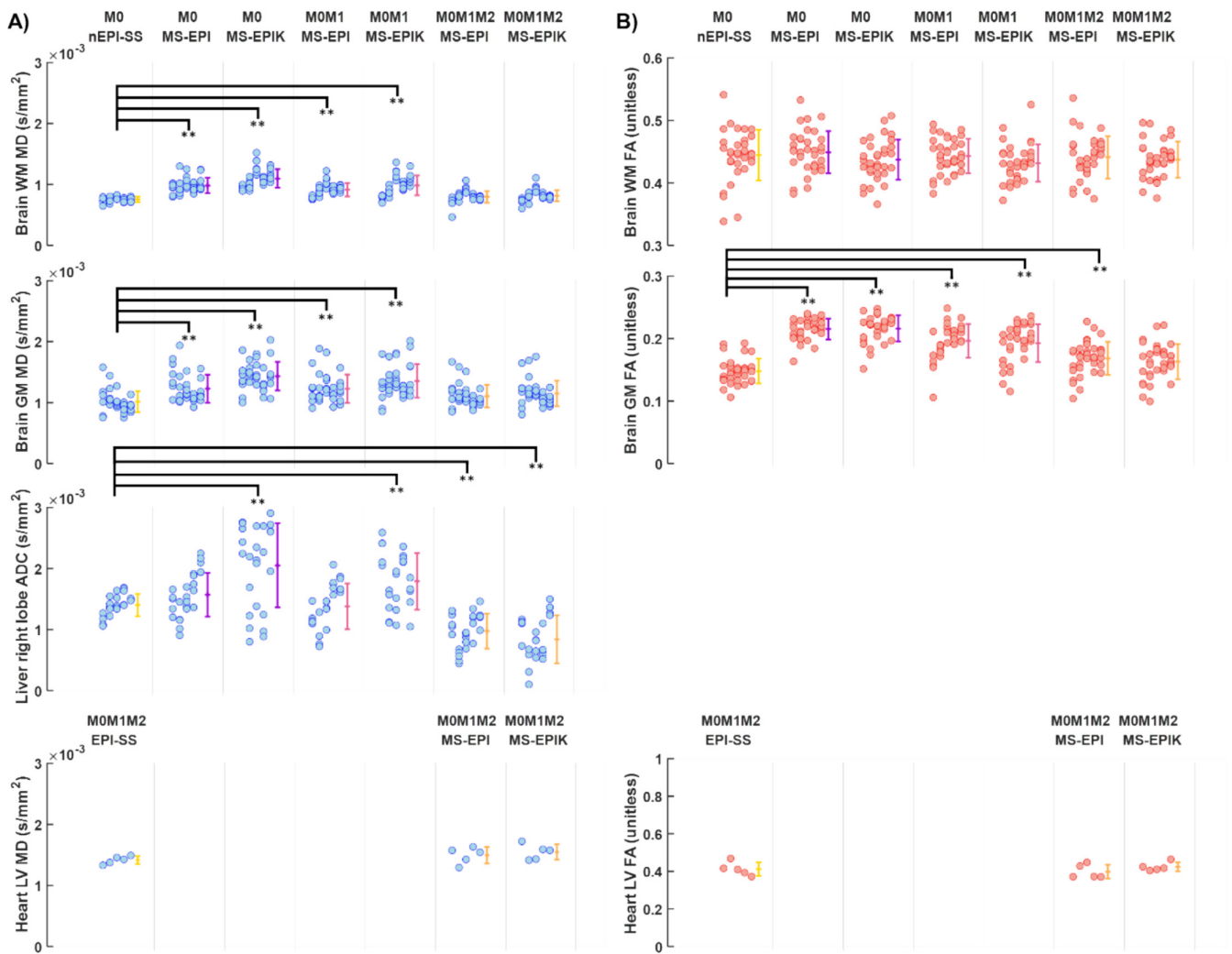
FIGURE 6 | Quantitative values across slices and volunteers in the brain, liver, and heart for the non-motion–compensated (M_0) and motion-compensated (M_0M_1 and $M_0M_1M_2$) diffusion encoding waveforms and for the single-shot EPI (SS-EPI), multi-shot EPI (MS-EPI) and EPIK (MS-EPIK) acquisitions. (A) Mean diffusivity (MD) in the Brain and Heart and Apparent Diffusion Coefficient (ADC) in the Liver. (B) Fraction of anisotropy (FA) in the Brain and Heart. Each scatter data point corresponds to a mean value measured in a single slice for a given volunteer. Scatter data are organized per subject. Statistical differences were evaluated using an ANOVA considering the SS-EPI acquisition as a reference scan. Significant p-values < 0.01 are represented by (**).

5 | Discussion

In this work, prospective strategies for mitigating artifacts in DWI MS-EPI were assessed. Motion-compensated diffusion encoding waveforms as well as an MS-EPIK readout were studied in silico and in vivo in the brain, liver, and heart. In silico, aliasing artifacts arising from inter-shot phase-variation and acceleration factors were evaluated for MS-EPI and MS-EPIK as well as their B_0 sensitivity. In addition, the inter-shot phase-variation across diffusion encoding waveform was studied in vivo using the keyhole of the MS-EPIK readout. Quantitative diffusion metrics and SNR of different reconstruction methods were also compared for each approach. First & second order motion-compensated diffusion encoding waveforms ($M_0M_1M_2$) were found to robustly reduce inter-shot phase variation and enable DWI MS-EPI in vivo for a range of applications.

Motion-compensated diffusion-encoding waveforms have previously been proposed to reduce motion-induced signal dropout in cardiac diffusion imaging [28,29]. These waveforms are constructed to null the phase contribution of moving spins with constant velocity and/or constant acceleration. In this work, using the keyhole region of the MS-EPIK readout in vivo, we were able to demonstrate that shot-to-shot phase variations were mostly due to physiologic motion which can be compensated by waveforms designed using the GMN theory. We also showed that the $M_0M_1M_2$ motion-compensated waveforms reduced the inter-shot phase variation compared to M_0 or M_0M_1 waveforms in the brain and liver. In the liver, the inter-shot phase CV remained elevated using $M_0M_1M_2$ likely because of uncorrected respiratory through-plane motion since the liver acquisitions were realized in free-breathing conditions.
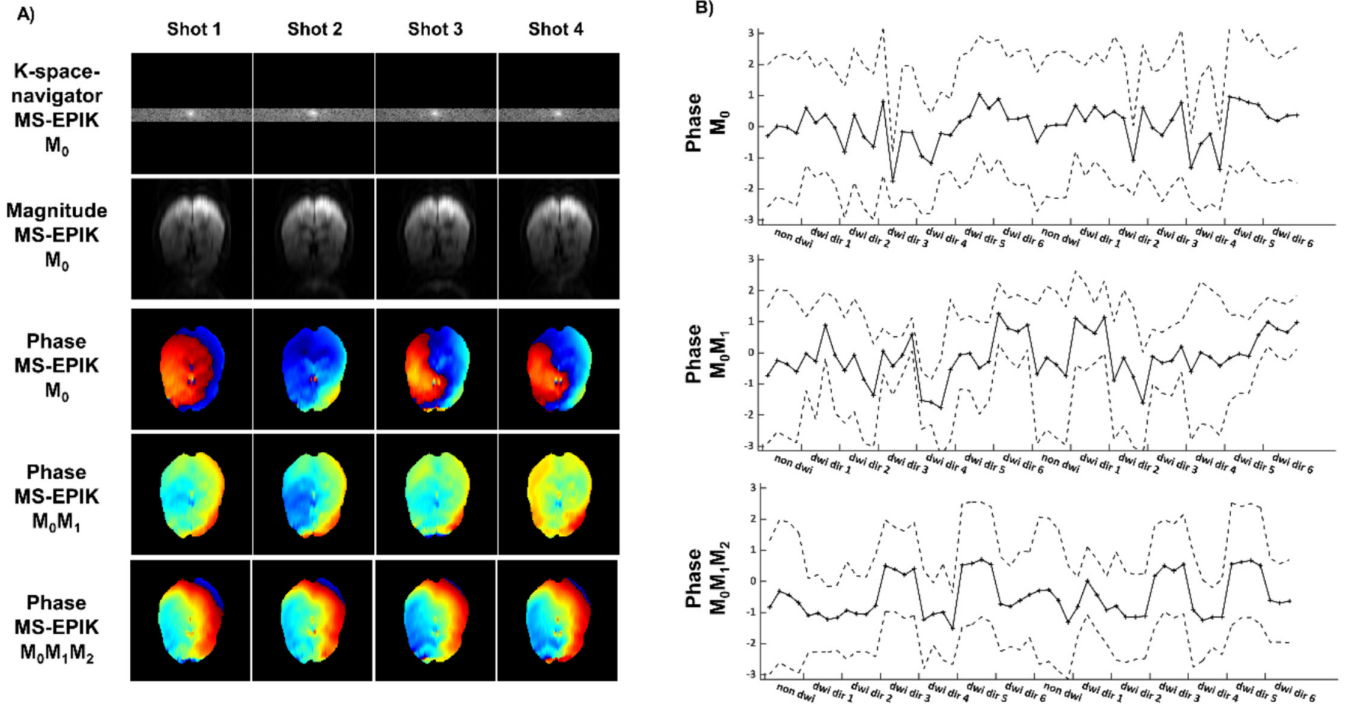
FIGURE 7 | In vivo shot-to-shot phase variation analysis using the keyhole region of the multi-shot EPIK (MS-EPIK) readout. (A) K-space of the keyhole region and corresponding magnitude and phase for each individual shot and for the non-motion compensated (M_0) and motion compensated (M_0M_1 and $M_0M_1M_2$) diffusion encoding waveforms. (B) Mean and standard deviation of the phase within the ROI for each diffusion direction, each average of the diffusion-weighted images (DWI) and non-DWI, and for the M_0, M_0M_1, and $M_0M_1M_2$ waveforms. Inter-shot phase variations were observed for M_0 and M_0M_1 waveforms while lower variations were obtained across the four shots using $M_0M_1M_2$.

The design of motion compensated waveforms using the GMN approach led to a significant increase in TE compared to a non-motion compensated waveform for an equivalent b-value. Numerical designs have been proposed [25,45] to reduce the TE contribution of the motion-compensated diffusion encoding waveforms. These numerical designs optimize the dead time in the symmetric diffusion encoding waveforms due to a high T_{preTE} (Figure 1). Using a higher R reduces T_{preTE} and thus reduces the benefit of using a numerically designed diffusion encoding waveform. An alternative solution is also to employ other readouts like spiral [46] that provide a $T_{preTE} = 0$ and trade geometric distortion for signal blurring. In this work, despite the increased TE, we showed that using $M_0M_1M_2$ waveforms with MS-EPI grants higher SNR benefits than using highly accelerated single-shot acquisition with M_0 diffusion encoding.

The EPIK approach was originally proposed as a single-shot approach offering a narrower Point Spread Function (PSF) than traditional SS-EPI, but lower than MS-EPI [31]. Here we evaluated an MS-EPIK approach which is robust to image aliasing as shown in silico. This was observed in vivo wherein the MS-EPIK readout displayed less signal aliasing (either due to motion or to an acceleration factor) than the MS-EPI readout for an equivalent diffusion encoding waveform. In the B_0 inhomogeneity analysis, an RMSE of ~15% was obtained for the MS-EPIK for $N_{shot} = 2,4,8$ readouts which were equivalent to the RMSE of the MS-EPI readout with $N_{shot} = 2$ (14%). MS-EPIK also showed equivalent image distortion as the SS-EPI readout in vivo. Here again, this corresponds to the *in silico* simulation since the

SS-EPI was acquired with $R = 2$ which has the same number of k-space lines as an MS-EPI $N_{shot} = 2$ trajectory.

For the "naïve" reconstructions in vivo, all the methods were compared with equivalent scan times by adjusting the number of averages, the acceleration factor, and the number of shots for the SS-EPI ($N_{shot} = 1$, $R = 2$, $N_{avg} = 8$), MS-EPI, and MS-EPIK readouts ($N_{shot} = 4$, $R = 1$, $N_{avg} = 2$). Quantitatively, the MD, FA, and ADC values measured in vivo using the reference SS-EPI readout were in the range of healthy values seen from literature in the brain [47], liver [4], and heart [48]. For the naïve reconstruction of MS-EPI and MS-EPIK, the inter-shot phase-induced aliasing artificially increased MD, FA, and ADC. For the MD parameter, only the acquisitions using $M_0M_1M_2$ showed no statistical differences compared to the SS-EPI. In the liver, the ADC obtained with the $M_0M_1M_2$ diffusion encoding waveform was significantly lower than using the M_0 SS-EPI. This is due to the perfusion/IVIM effect being compensated with the motion-corrected diffusion encoding waveform [26,49], artificially reducing the ADC between M_0, M_0M_1, and $M_0M_1M_2$ acquisitions. This effect was not observed in the brain, probably due to the lower perfusion fraction, nor in the heart since $M_0M_1M_2$ waveforms were used in both the SS and MS acquisitions.

For the reconstructions with an acceleration factor, only a subset of shots from the N_{shot} were used which led to different k-space sampling factors across the readouts and were not studied at matching scan-time. For instance, in this work, a $R = 4$ corresponds to 18.75% of the k-space being sampled for an MS-EPI acquisition (24 lines sampled/shot, PF 75%, matrix 128×128) but
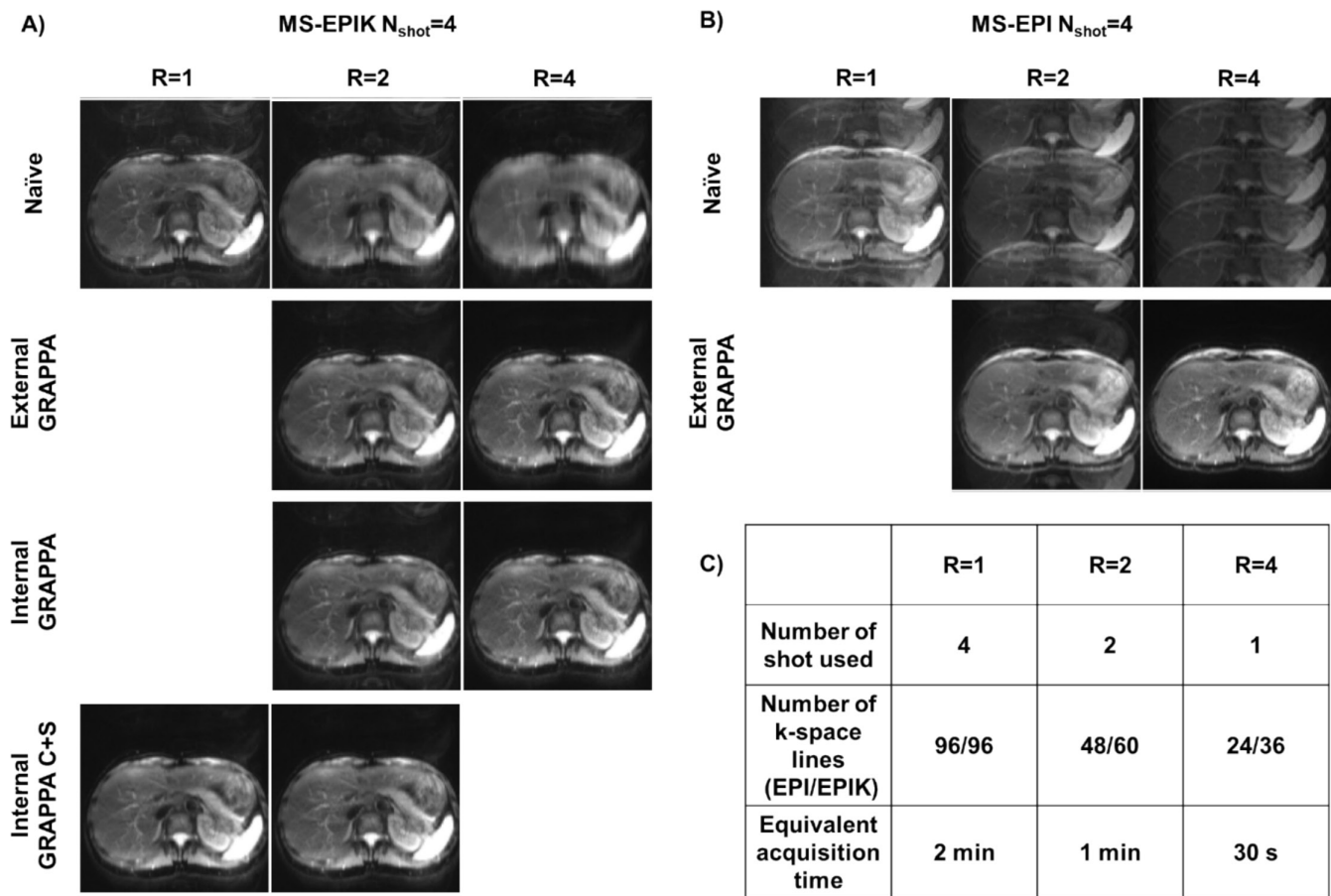
FIGURE 8 | Example of in vivo liver acquisition in one volunteer using the first- & second-order motion compensated ($M_0M_1M_2$) diffusion encoding waveforms. (A) Reconstruction of Multi-shot EPI with keyhole (MS-EPIK) readout with the Naïve, internal, external GRAPPA, and GRAPPA C + S methods for several acceleration factors (R). (B) Multi-shot EPI (MS-EPI) images were reconstructed with the naïve and external GRAPPA methods. (C) Number of k-space lines used and equivalent acquisition time for a reconstruction given R. For the GRAPPA C + S, the case R = 1 corresponds to a shot-to-shot phase mitigation reconstruction, and the case R = 4 is equivalent to the internal GRAPPA reconstruction. Overall MS-EPIK acquisitions display lower aliasing than MS-EPI. Image aliasing due to shot-to-shot phase variation can still be observed in external GRAPPA reconstruction of the MS-EPI at R = 2. The internal GRAPPA C + S successfully mitigates inter-shot phase variation at R = 1 for the MS-EPIK readout.

up to 28.1% for an MS-EPIK trajectory (36 lines sampled/shot, PF 75%, matrix 128×128). In comparison, the referenced SS-EPI protocol used here sampled 37.5% of the k-space using R = 2 (48 lines sampled, PF 75%, Matrix 128×128). We also compared external GRAPPA and internal GRAPPA and GRAPPA C + S reconstruction methods since the keyhole region of the MS-EPIK can also be seen as integrated ACS lines. The GRAPPA C + S used here was an integrated version of the realigned GRAPPA reconstruction proposed by Liu et al. [35] to mitigate shot-to-shot phase variation for MS-EPI. In silico, overall, a lower RMSE was obtained using the MS-EPIK readout compared to the MS-EPI while equivalent SNR was obtained between both readouts in vivo. Reconstruction methods were equivalent in silico while in vivo the GRAPPA C + S reconstruction provided a slightly higher SNR in the brain. Across all reconstructions, $R < N_{shot}$, using motion-compensated waveforms increased the SNR while at $R = N_{shot}$ only one shot was considered, and non-motion compensated waveforms provided higher SNR. In vivo at high R equivalent SNR was measured between MS-EPI and MS-EPIK while a lower RMSE was obtained for the MS-EPIK *in silico*.

6 | Limitations

This study had several limitations. First, only protocols with $N_{shot} = 4$ were evaluated in vivo for MS-EPI and MS-EPIK with a limited spatial coverage, multiple parameters matching across organs and considering the SS-EPI as a reference scan. SS-EPI acquisitions suffered from strong image distortion and required parallel imaging to obtain low T_{preTE} and TE. Second, the results of this manuscript were demonstrated only on a small sample size ($N = 5$) across three organs. Single organ studies with larger sample sizes and sequence parameters adjusted per organ are necessary to confirm the findings. Third, partial Fourier was not directly studied even though it is an important mechanism to reduce T_{Epi} and T_{preTE} for SS-EPI. As shown in Figure 1, partial Fourier becomes less advantageous as the N_{shot} increases. Here, all the acquisitions and simulations were performed using a constant partial Fourier factor of 75%. Fourth, the T2 and T2* relaxations were not simulated and evaluated between SS-EPI, MS-EPI, and MS-EPIK. T2/T2* relaxation during the EPI readout induces blurring which increases as the T_{Epi} increases and
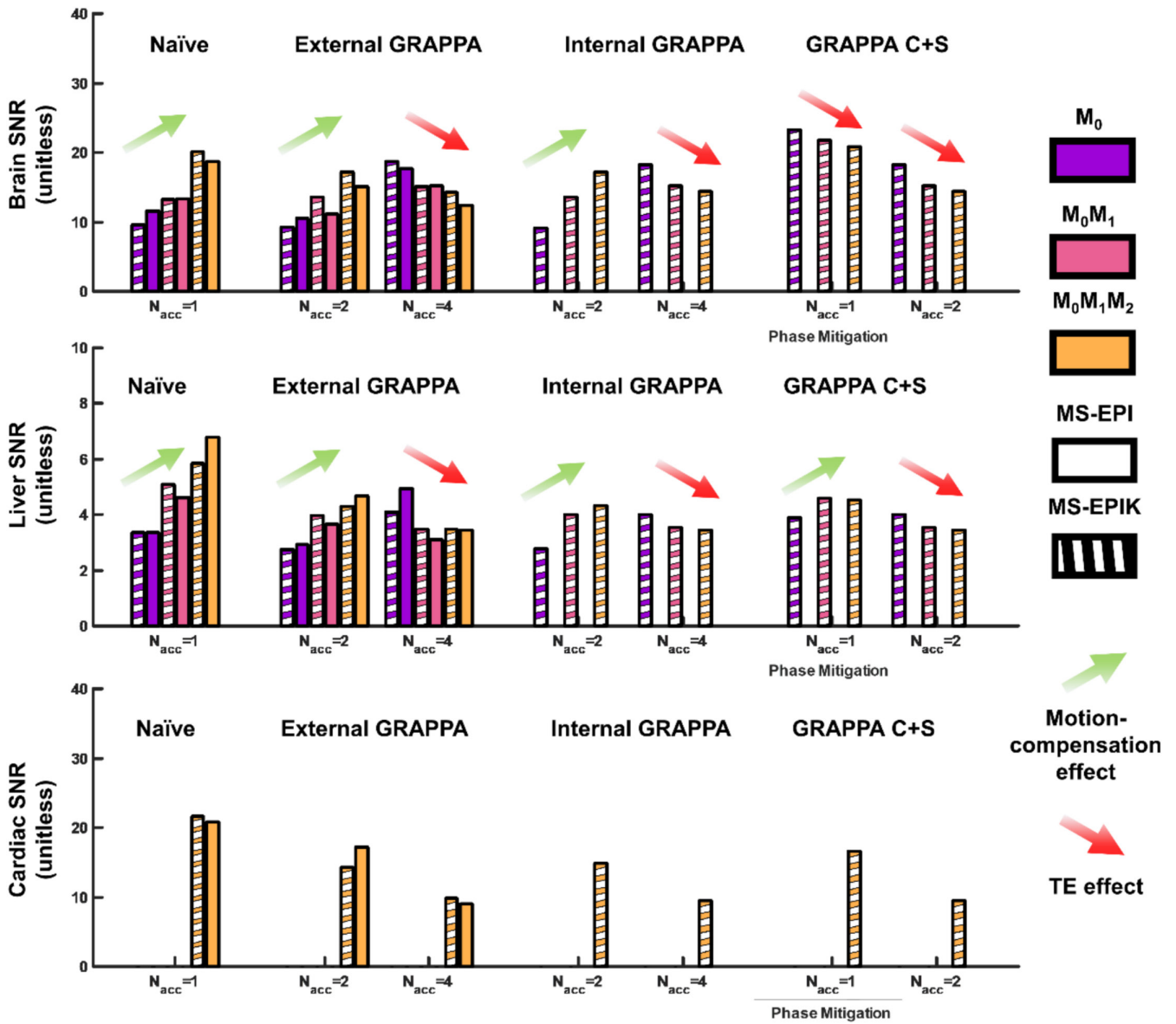
FIGURE 9 | In vivo acceleration SNR analysis. SNR values across slices and across volunteers in the brain, liver, and heart for several acceleration factors (R) reconstructed with the Naïve, internal, external GRAPPA, and GRAPPA C + S, for the non-motion compensated (M_0) and motion compensated (M_0M_1 and $M_0M_1M_2$) diffusion encoding waveforms and for the single-shot EPI (SS-EPI) and multi-shot EPI (MS-EPI) and EPIK (MS-EPIK) acquisitions. For the GRAPPA C + S, the case R = 1 corresponds to a shot-to-shot phase mitigation reconstruction, and the case R = 4 is equivalent to the internal GRAPPA reconstruction. The green arrow represents the gain in SNR across diffusion-encoding waveforms due to motion compensation. The red arrow represents the SNR loss across diffusion-encoding waveforms due to the increased TE.

accounts for most of the PSF differences between SS-EPI, MS-EPI, and MS-EPIK [31,50]. Finally, only a few properties of the MS-EPIK readout were evaluated in this work. MS-EPIK has been initially proposed for DWI as a navigator-integrated MS DWI approach [32] to correct inter-shot phase variation which was not evaluated here.

7 | Conclusion

In this study, MS-EPIK offered limited benefit to reduce signal aliasing compared to MS-EPI in vivo and had comparable image distortion as SS-EPI. $M_0M_1M_2$ waveforms were shown to mitigate shot-to-shot phase variation for MS-EPI in the brain, liver,

and heart. In the liver, $M_0M_1M_2$ waveforms lead to significantly lower diffusivities compared to M_0 waveforms due to motion-compensated perfusion signal.

Data Availability Statement

The data that support the findings of this study are available from the corresponding author upon reasonable request.

References

1. R. Bammer, "Basic Principles of Diffusion-Weighted Imaging," *European Journal of Radiology* 45, no. 3 (2003): 169–184, https://doi.org/10.1016/S0720-048X(02)00303-0.

2. K. Moulin, P. Croisille, T. Feiweier, et al., "In Vivo Free-Breathing DTI and IVIM of the Whole Human Heart Using a Real-Time Slice-Followed SE-EPI Navigator-Based Sequence: A Reproducibility Study in Healthy Volunteers," *Magnetic Resonance in Medicine* 76, no. 1 (2016): 70–82, https://doi.org/10.1002/mrm.25852.

3. D. Le Bihan and H. Johansen-Berg, "Diffusion MRI at 25: Exploring Brain Tissue Structure and Function," *NeuroImage* 61, no. 2 (2012): 324–341, https://doi.org/10.1016/j.neuroimage.2011.11.006.

4. P. G. Kele, "Diffusion Weighted Imaging in the Liver," *WJG* 16, no. 13 (2010): 1567–1576, https://doi.org/10.3748/wjg.v16.i13.1567.

5. P. Jezzard and R. S. Balaban, "Correction for Geometric Distortion in Echo Planar Images From B0 Field Variations," *Magnetic Resonance in Medicine* 34, no. 1 (1995): 65–73, https://doi.org/10.1002/mrm.1910340111.

6. P. Jezzard and S. Clare, "Sources of Distortion in Functional MRI Data," *Human Brain Mapping* 8, no. 2–3 (1999): 80–85, https://doi.org/10.1002/(SICI)1097-0193(1999)8:2/3<80::AID-HBM2>3.0.CO;2-C.

7. J. A. McKay, S. Moeller, L. Zhang, E. J. Auerbach, M. T. Nelson, and P. J. Bolan, "Nyquist Ghost Correction of Breast Diffusion Weighted Imaging Using Referenceless Methods," *Magnetic Resonance in Medicine* 81, no. 4 (2019): 2624–2631, https://doi.org/10.1002/mrm.27563.

8. N. Chen and A. M. Wyrwicz, "Removal of EPI Nyquist Ghost Artifacts With two-Dimensional Phase Correction," *Magnetic Resonance in Medicine* 51, no. 6 (2004): 1247–1253, https://doi.org/10.1002/mrm.20097.

9. M. H. Buonocore and L. Gao, "Ghost Artifact Reduction for Echo Planar Imaging Using Image Phase Correction," *Magnetic Resonance in Medicine* 38, no. 1 (1997): 89–100, https://doi.org/10.1002/mrm.1910380114.

10. R. J. H. van Gorkum, C. von Deuster, C. Guenthner, C. T. Stoeck, and S. Kozerke, "Analysis and Correction of off-Resonance Artifacts in Echo-Planar Cardiac Diffusion Tensor Imaging," *Magnetic Resonance in Medicine* 84, no. 5 (2020): 2561–2576, https://doi.org/10.1002/mrm.28318.

11. M. O. Irfanoglu, P. Modi, A. Nayak, E. B. Hutchinson, J. Sarlls, and C. Pierpaoli, "DR-BUDDI (Diffeomorphic Registration for Blip-Up Blip-Down Diffusion Imaging) Method for Correcting Echo Planar Imaging Distortions," *NeuroImage* 106 (2015): 284–299, https://doi.org/10.1016/j.neuroimage.2014.11.042.

12. C. Liao, B. Bilgic, Q. Tian, et al., "Distortion-Free, High-Isotropic-Resolution Diffusion MRI With gSlider BUDA-EPI and Multicoil Dynamic B_0 Shimming," *Magnetic Resonance in Medicine* 86, no. 2 (2021): 791–803, https://doi.org/10.1002/mrm.28748.

13. M. A. Griswold, P. M. Jakob, R. M. Heidemann, et al., "Generalized Autocalibrating Partially Parallel Acquisitions (GRAPPA)," *Magnetic Resonance in Medicine* 47, no. 6 (2002): 1202–1210, https://doi.org/10.1002/mrm.10171.

14. K. P. Pruessmann, M. Weiger, M. B. Scheidegger, and P. Boesiger, "SENSE: Sensitivity Encoding for Fast MRI," *Magnetic Resonance in Medicine* 42, no. 5 (1999): 952–962, https://doi.org/10.1002/(SICI)1522-2594(199911)42:5<952::AID-MRM16>3.0.CO;2-S.

15. D. A. Porter and R. M. Heidemann, "High Resolution Diffusion-Weighted Imaging Using Readout-Segmented Echo-Planar Imaging, Parallel Imaging and a Two-Dimensional Navigator-Based Reacquisition: EPI With Parallel Imaging and 2D Reacquisition," *Magnetic Resonance in Medicine* 62, no. 2 (2009): 468–475, https://doi.org/10.1002/mrm.22024.

16. K. Butts, S. J. Riederer, R. L. Ehman, R. M. Thompson, and C. R. Jack, "Interleaved Echo Planar Imaging on a Standard MRI System," *Magnetic Resonance in Medicine* 31, no. 1 (1994): 67–72, https://doi.org/10.1002/mrm.1910310111.

17. K. L. Miller and J. M. Pauly, "Nonlinear Phase Correction for Navigated Diffusion Imaging," *Magnetic Resonance in Medicine* 50, no. 2 (2003): 343–353, https://doi.org/10.1002/mrm.10531.

18. D. Atkinson, D. A. Porter, D. L. G. Hill, F. Calamante, and A. Connelly, "Sampling and Reconstruction Effects due to Motion in Diffusion-Weighted Interleaved Echo Planar Imaging," *Magnetic Resonance in Medicine* 44, no. 1 (2000): 101–109, https://doi.org/10.1002/1522-2594(200007)44:1<101::AID-MRM15>3.0.CO;2-S.

19. N. Chen, A. Guidon, H. C. Chang, and A. W. Song, "A Robust Multi-Shot Scan Strategy for High-Resolution Diffusion Weighted MRI Enabled by Multiplexed Sensitivity-Encoding (MUSE)," *NeuroImage* 72 (2013): 41–47, https://doi.org/10.1016/j.neuroimage.2013.01.038.

20. M. Mani, M. Jacob, D. Kelley, and V. Magnotta, "Multi-Shot Sensitivity-Encoded Diffusion Data Recovery Using Structured Low-Rank Matrix Completion (MUSSELS)," *Magnetic Resonance in Medicine* 78, no. 2 (2017): 494–507, https://doi.org/10.1002/mrm.26382.

21. Y. Hu, D. M. Ikeda, S. M. Pittman, et al., "Multishot Diffusion-Weighted MRI of the Breast With Multiplexed Sensitivity Encoding (MUSE) and Shot Locally Low-Rank (Shot-LLR) Reconstructions," *Journal of Magnetic Resonance Imaging* 53, no. 3 (2021): 807–817, https://doi.org/10.1002/jmri.27383.

22. F. Hennel, "Image-Based Reduction of Artifacts in Multishot Echo-Planar Imaging," *Journal of Magnetic Resonance* 134, no. 2 (1998): 206–213, https://doi.org/10.1006/jmre.1998.1502.

23. D. A. Feinberg and K. Oshio, "Phase Errors in Multi-Shot Echo Planar Imaging," *Magnetic Resonance in Medicine* 32, no. 4 (1994): 535–539, https://doi.org/10.1002/mrm.1910320418.

24. J. L. Duerk and O. P. Simonetti, "Review of MRI Gradient Waveform Design Methods With Application in the Study of Motion," *Concepts in Magnetic Resonance* 5, no. 2 (1993): 105–122, https://doi.org/10.1002/cmr.1820050202.

25. E. Aliotta, H. H. Wu, and D. B. Ennis, "Convex Optimized Diffusion Encoding (CODE) Gradient Waveforms for Minimum Echo Time and Bulk Motion–Compensated Diffusion-Weighted MRI," *Magnetic Resonance in Medicine* 77, no. 2 (2017): 717–729, https://doi.org/10.1002/mrm.26166.

26. K. Moulin, E. Aliotta, and D. B. Ennis, "Effect of Flow-Encoding Strength on Intravoxel Incoherent Motion in the Liver," *Magnetic Resonance in Medicine* 81, no. 3 (2019): 1521–1533, https://doi.org/10.1002/mrm.27490.

27. S. S. Rauh, A. J. Riexinger, S. Ohlmeyer, et al., "A Mixed Waveform Protocol for Reduction of the Cardiac Motion Artifact in Black-Blood Diffusion-Weighted Imaging of the Liver," *Magnetic Resonance Imaging* 67 (2020): 59–68, https://doi.org/10.1016/j.mri.2019.12.011.

28. C. T. Stoeck, C. von Deuster, M. Genet, D. Atkinson, and S. Kozerke, "Second-Order Motion-Compensated Spin Echo Diffusion Tensor Imaging of the Human Heart," *Magnetic Resonance in Medicine* 75, no. 4 (2016): 1669–1676, https://doi.org/10.1002/mrm.25784.

29. C. L. Welsh, E. V. R. DiBella, and E. W. Hsu, "Higher-Order Motion-Compensation for In Vivo Cardiac Diffusion Tensor Imaging in Rats," *IEEE Transactions on Medical Imaging* 34, no. 9 (2015): 1843–1853, https://doi.org/10.1109/TMI.2015.2411571.

30. Moulin K, Verzhbinsky IA, Maforo NG, Perotti LE, Ennis DB. Probing Cardiomyocyte Mobility With Multi-Phase Cardiac Diffusion Tensor MRI. Lionetti V, ed. *PLoS ONE*. 2020;15(11):e0241996, https://doi.org/10.1371/journal.pone.0241996.

31. M. Zaitsev, K. Zilles, and N. J. Shah, "Shared k-Space Echo Planar Imaging With Keyhole," *Magnetic Resonance in Medicine* 45, no. 1 (2001): 109–117, https://doi.org/10.1002/1522-2594(200101)45:1<109::AID-MRM1015>3.0.CO;2-X.

32. R. G. Nunes, P. Jezzard, T. E. J. Behrens, and S. Clare, "Self-Navigated Multishot Echo-Planar Pulse Sequence for High-Resolution Diffusion-Weighted Imaging," *Magnetic Resonance in Medicine* 53, no. 6 (2005): 1474–1478, https://doi.org/10.1002/mrm.20499.

33. S. D. Yun, M. Reske, K. Vahedipour, T. Warbrick, and N. J. Shah, "Parallel Imaging Acceleration of EPIK for Reduced Image Distortions in fMRI," *NeuroImage* 73 (2013): 135–143, https://doi.org/10.1016/j.neuroimage.2013.01.070.

34. M. Zaitsev, J. D'Arcy, D. J. Collins, M. O. Leach, K. Zilles, and N. J. Shah, "Dual-Contrast Echo Planar Imaging With Keyhole: Application to Dynamic Contrast-Enhanced Perfusion Studies," *Physics in Medicine and Biology* 50, no. 19 (2005): 4491–4505, https://doi.org/10.1088/0031-9155/50/19/005.

35. W. Liu, X. Zhao, Y. Ma, X. Tang, and J. H. Gao, "DWI Using Navigated Interleaved Multishot EPI With Realigned GRAPPA Reconstruction," *Magnetic Resonance in Medicine* 75, no. 1 (2016): 280–286, https://doi.org/10.1002/mrm.25586.

36. U. Gamper, P. Boesiger, and S. Kozerke, "Diffusion Imaging of the in Vivo Heart Using Spin Echoes–Considerations on Bulk Motion Sensitivity," *Magnetic Resonance in Medicine* 57, no. 2 (2007): 331–337, https://doi.org/10.1002/mrm.21127.

37. I. Mekkaoui, K. Moulin, P. Croisille, J. Pousin, and M. Viallon, "Quantifying the Effect of Tissue Deformation on Diffusion-Weighted MRI: A Mathematical Model and an Efficient Simulation Framework Applied to Cardiac Diffusion Imaging," *Physics in Medicine and Biology* 61, no. 15 (2016): 5662–5686, https://doi.org/10.1088/0031-9155/61/15/5662.

38. G. McGibney, M. R. Smith, S. T. Nichols, and A. Crawley, "Quantitative Evaluation of Several Partial Fourier Reconstruction Algorithms Used in MRI," *Magnetic Resonance in Medicine* 30, no. 1 (1993): 51–59, https://doi.org/10.1002/mrm.1910300109.

39. V. J. Wedeen, R. M. Weisskoff, and B. P. Poncelet, "MRI Signal Void Due to In-Plane Motion Is All-or-None," *Magnetic Resonance in Medicine* 32, no. 1 (1994): 116–120, https://doi.org/10.1002/mrm.1910320116.

40. L. A. Shepp and B. F. Logan, "The Fourier Reconstruction of a Head Section," *IEEE Transactions on Nuclear Science* 21, no. 3 (1974): 21–43, https://doi.org/10.1109/TNS.1974.6499235.

41. Chow K, Kellman P, Xue H. "Prototyping Image Reconstruction and Analysis With FIRE," in *Proceedings SCMR 24th Annual Scientific Sessions, Virtual Meeting* (2021).

42. T. Liu, H. Li, K. Wong, A. Tarokh, and L. Guo, "Brain Tissue Segmentation Based on DTI Data," *Neuroimage* 38, no. 1 (2007): 114–123, https://doi.org/10.1016/j.neuroimage.2007.07.002.

43. T. Zhang, J. M. Pauly, S. S. Vasanawala, and M. Lustig, "Coil Compression for Accelerated Imaging With Cartesian Sampling," *Magnetic Resonance in Medicine* 69, no. 2 (2013): 571–582, https://doi.org/10.1002/mrm.24267.

44. F. L. Goerner and G. D. Clarke, "Measuring Signal-to-Noise Ratio in Partially Parallel Imaging MRI," *Medical Physics* 38, no. 9 (2011): 5049–5057, https://doi.org/10.1118/1.3618730.

45. M. J. Middione, M. Loecher, K. Moulin, and D. B. Ennis, "Optimization Methods for Magnetic Resonance Imaging Gradient Waveform Design," *NMR in Biomedicine* 33, no. 12 (2020): e4308, https://doi.org/10.1002/nbm.4308.

46. M. Gorodezky, A. D. Scott, P. F. Ferreira, S. Nielles-Vallespin, D. J. Pennell, and D. N. Firmin, "Diffusion Tensor Cardiovascular Magnetic Resonance With a Spiral Trajectory: An In Vivo Comparison of Echo Planar and Spiral Stimulated Echo Sequences," *Magnetic Resonance in Medicine* 80, no. 2 (2018): 648–654, https://doi.org/10.1002/mrm.27051.

47. U. Löbel, J. Sedlacik, D. Güllmar, W. A. Kaiser, J. R. Reichenbach, and H. J. Mentzel, "Diffusion Tensor Imaging: The Normal Evolution of ADC, RA, FA, and Eigenvalues Studied in Multiple Anatomical Regions of the Brain," *Neuroradiology* 51, no. 4 (2009): 253–263, https://doi.org/10.1007/s00234-008-0488-1.

48. K. Moulin, C. T. Stoeck, L. Axel, et al., "In Vivo Cardiac Diffusion Imaging Without Motion-Compensation Leads to Unreasonably High Diffusivity," *Journal of Magnetic Resonance Imaging* 58, no. 6 (2023): 1990–1991, https://doi.org/10.1002/jmri.28703.

49. A. Wetscherek, B. Stieltjes, and F. B. Laun, "Flow-Compensated Intravoxel Incoherent Motion Diffusion Imaging," *Magnetic Resonance in Medicine* 74, no. 2 (2015): 410–419, https://doi.org/10.1002/mrm.25410.

50. M. A. Bernstein, K. F. King, and J. Z. Xiaohong, *Handbook of MRI Pulse Sequences* (Elsevier, 2004).

Supporting Information

Additional supporting information can be found online in the Supporting Information section.